WILEY

SHORT COMMUNICATION OPEN ACCESS

Infrared Thermography of Turbulence Patterns of Operational Wind Turbine Rotor Blades Supported With High-Resolution Photography: KI-VISIR Dataset

Somsubhro Chaudhuri[1] | Michael Stamm[1] | Ivana Lapšanská[1] | Thibault Lançon[1] | Lars Osterbrink[2] | Thomas Driebe[2] | Daniel Hein[2] | René Harendt[3]

[1]8.3 Thermographic Methods, Bundesanstalt für Materialforschung und -prüfung (BAM), Berlin, Germany | [2]LATODA (Adoxin UG), Hamburg/Marburg, Germany | [3]ROMOTIONCAM™ GmbH, Berlin, Germany

Correspondence: Somsubhro Chaudhuri (somsubhro.chaudhuri@bam.de)

ABSTRACT

With increasing wind energy capacity and installation of wind turbines, new inspection techniques are being explored to examine wind turbine rotor blades, especially during operation. A common result of surface damage phenomena (such as leading edge erosion) is the premature transition of laminar to turbulent flow on the surface of rotor blades. In the KI-VISIR (Künstliche Intelligenz Visuell und Infrarot Thermografie—Artificial Intelligence-Visual and Infrared Thermography) project, infrared thermography is used as an inspection tool to capture so-called thermal turbulence patterns (TTPs) that result from such surface contamination or damage. To complement the thermographic inspections, high-resolution photography is performed to visualise, in detail, the sites where these turbulence patterns initiate. A convolutional neural network (CNN) was developed and used to detect and localise turbulence patterns. A unique dataset combining the thermograms and visual images of operational wind turbine rotor blades has been provided, along with the simplified annotations for the turbulence patterns. Additional tools are available to allow users to use the data requiring only basic Python programming skills.

1 | Introduction

To achieve global carbon neutrality goals, the number of wind turbines in operation and construction is exponentially increasing, with a capacity of 906 GW worldwide in 2022 [1]. The rotor blades of wind turbines are aerodynamic structures that convert the kinetic energy of the wind into torque, which is then used to generate electricity. For efficient conversion, the blades are designed for optimal laminar flow in the given wind conditions. Based on the aerofoil shape (which changes along the blade length) and angle of attack (the angle at which the incoming flow meets the leading edge of the blade), there

is an optimal transition line after which laminar flow transitions to turbulent flow. This has been extensively studied and simulated in literature [2–4]. However, because of surface dirt/irregularity/roughness/damage, especially at the leading edge of the blade, the laminar flow may prematurely transition to turbulent flow, effectively reducing the aerodynamic performance of the blade at that location [5]. Numerous studies investigate different phenomena that cause such damage, such as airborne particles and rain [6–9], and methods to protect blades against such damage [10]. Based on real damage profiles and simulation studies, it has been estimated that the loss of annual energy production (AEP) is approximately

---

2%–3.7%, depending on the extent of damage [11]. To detect leading edge erosion remotely, multiple techniques are being investigated, with a recent study on detecting far-field aerodynamic noise (generated due to turbulent flow) [12]. Another non-contact technique that is frequently examined, and was employed in this study, is infrared thermography [6, 7, 13–15]. The nature of turbulent flow is that it increases the interaction between the air flow and the surface of the rotating blade, which effectively increases the heat flux from the air into the blade and vice versa. If the temperature of the blade is different from the air (because of the radiation from the sun and diurnal temperature variations), the increased convection will cause a local temperature change in the blade. This change in temperature can be detected using a suitable infrared thermography camera that is sensitive to minute changes in temperature. The sensitivity of the thermal camera, commonly referred to as Noise Equivalent Temperature Difference (NETD), should be low enough to detect the induced temperature contrast, commonly in the shape of a wedge. A study of the influence of defect characteristics and aerofoil geometry on the detectability of the resulting wedges was performed by Jensen et al. [13]. Parrey et al. performed an investigation where a model was developed to automate the detection of the turbulence patterns in thermographic inspection data [16].

In the KI-VISIR—'Künstliche Intelligenz Visuell (Bilder) und Infrarot Thermografie' or 'Artificial Intelligence-Visual (images) and Infrared Thermography'—project, infrared thermography is used as a non-contact inspection technique to capture thermograms of rotating wind turbine rotor blades from pressure and suction sides at different positions (dependent on wind speed, wind direction and feasibility at the site). In order to corroborate the findings in the thermograms and identify potential sources of premature laminar to turbulence transition, high-resolution visual photographs are captured of the same blades and perspective by ROMOTIONCAM. The paper is structured as follows: Section 2 describes the methodology adopted to perform the inspections; Section 3 provides a description of the publicly available dataset comprising of the thermal and visual images, along with some additional tools to aid in understanding how the data is provided. The article concludes with Sections 4 and 5 that provide a discussion on the data and summarises the next steps, respectively.

2 | Methodology

2.1 | Field Inspection

In total, 30 onshore wind turbines were inspected both visually and with thermography from either suction or pressure side at various locations within Germany. The inspections were performed from the ground while the turbines were in operation. For the thermal data acquisition, a long-wavelength infrared camera (specifications provided in Table 1), mounted on a pan-tilt (positional head) unit (PTU), is used to sequentially scan the blades. The camera was panned from the hub to the root of a blade of a given turbine capturing one section of each blade at a time.

In conjunction with the thermographic inspection, a visual inspection with a high-resolution RGB camera was performed by ROMOTIONCAM at the same relative positioning to the turbine. The technology (patented [17]) of ROMOTIONCAM uses a video camera, which is used for motion detection, and a high-resolution photo camera with a telephoto lens installed in a rotating pan-tilt head that follows the movement of the rotor blades. The movement of the rotor is constantly monitored by the video camera during the inspection; specially developed software evaluates the frames, recognises the blade tips and creates a virtual model that is compared and synchronised with the movement of the rotor. These data are passed on to the rotating pan-tilt head in the form of movement data and guide the photo camera to selectable sections and angular positions in synchronisation with the movement of the rotor. With this technology, the rotor blade section is followed and captured visually, thus reducing motion blur and enabling the auto-focussing of the visual camera. The parameters of the camera are provided in Table 2. A schematic of both systems set up in the field is shown in Figure 1. Both systems are approximately 100–120 m away from the base of the wind turbine, with the distance depending on the length of the blade.

2.2 | AI-Based Detection

A state-of-the-art convolutional neural network (CNN) was developed for the automatic detection and localisation of thermographic turbulence patterns (TTPs) in thermographic images. CNNs are a

TABLE 1 | Specifications of the infrared camera used for inspections.

Infrared camera model	Detector	Wavelength	Detector resolution	NETD	Objective focal length	Maximum frame rate (at full frame)
InfraTec IR8800	Cooled $Hg_{1-x}Cd_xTe$ MCT Focal-Plane-Array	7.7–10.4 μm	512 × 640 pixel; pitch: 16 μm	< 30 mK	200 mm	200 Hz

TABLE 2 | ROMOTIONCAM camera parameters.

Photo camera sensor size	Pixels	Pixel pitch	Objective focal length	Ground sample distance (GSD)[a]
35.9 mm × 23.9 mm	45.7 MP (8256 × 5504 pixel)	4.345 μm	500 mm	0.869 mm/px ± 0.2 mm/px

[a]The GSD value varies because of the changes in distance during the movement of the rotor blades and recordings from different angular positions.

class of deep learning models specifically designed for processing data with a grid-like topology, such as images. CNNs are particularly well-suited for image detection tasks because of their ability to learn spatial hierarchies of features automatically and adaptively from input images. This characteristic enables CNNs to effectively identify and localise patterns within complex image data.

In the KI-VISIR project, a state-of-the-art YOLOv9 architecture was used, which is exemplarily depicted in Figure 2.

YOLOv9 is a single-stage object detection algorithm that analyses an image only once. It comprises a backbone for feature extraction, a neck that uses pyramid networks to combine features from multiple layers and multiple heads to detect objects at different resolutions. YOLOv9 adds an auxiliary section to improve training reliability by linking input data to target output, which counters information loss through deep learning layers. The code for YOLOv9 can be freely downloaded from
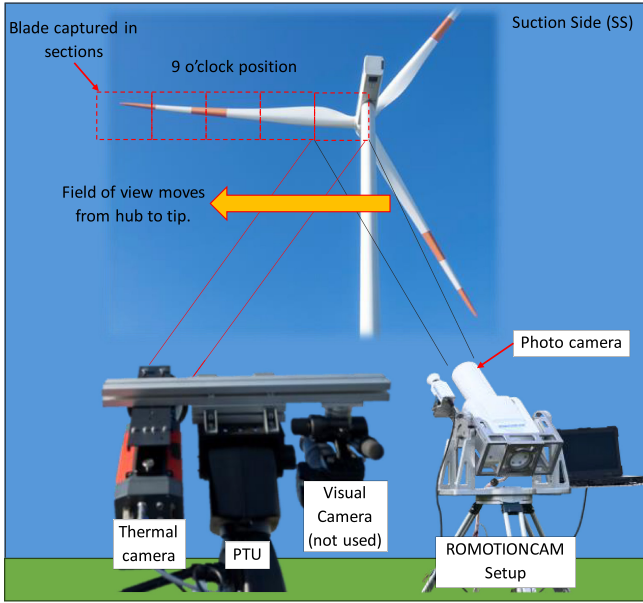

FIGURE 1 | Schematic of how the systems are set up on the field.
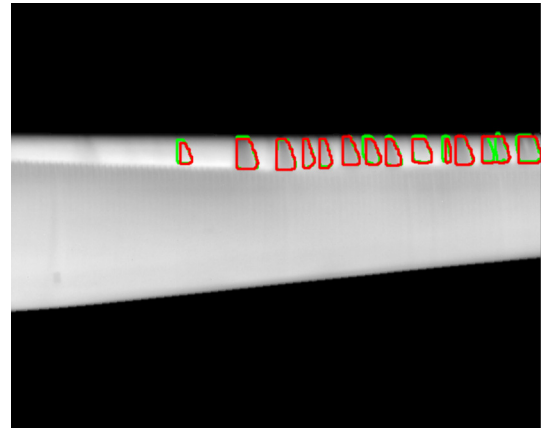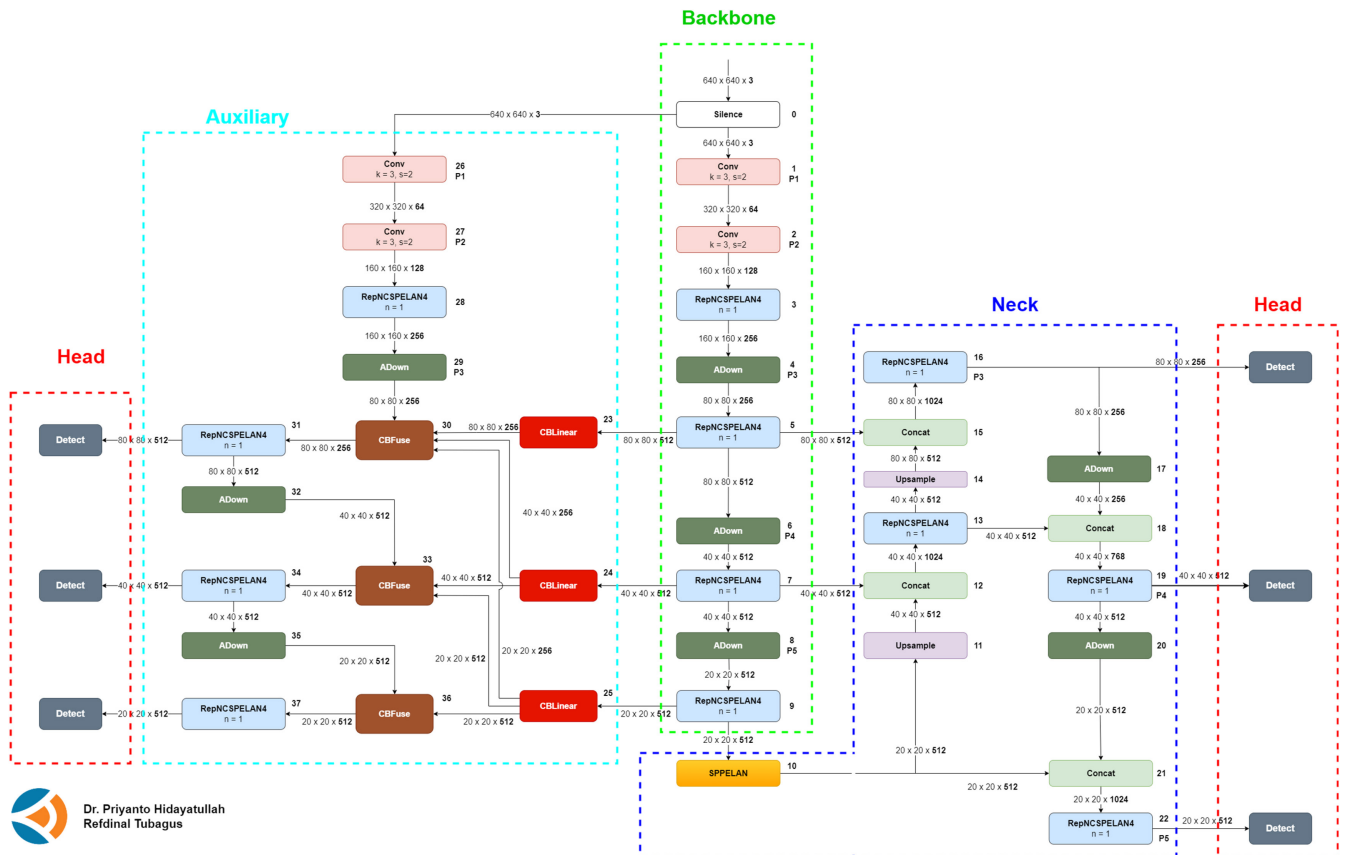

FIGURE 3 | Example thermal image with manual annotation (ground truth) shown in green and automated annotation in red.

FIGURE 2 | An example of a YOLOv9 architecture for image classification. Taken from [18].

GitHub at [19] and for more information it is recommended to read the accompanying paper [20]. In the KI-VISIR project, the developed model was designed for polygon detection, a specific type of object detection where the model identifies and draws polygon around regions of interest—in this case, the TTP areas. The CNN was trained and evaluated using a dataset comprising over 2000 thermographic images, each annotated by experienced annotators according to an internally determined and validated guideline. The training process involved feeding the CNN with these annotated images, allowing the model to learn the distinguishing features of TTP. Through iterative learning and optimisation, the CNN was able to generalise from the training data, thereby enhancing its ability to detect TTP in previously unseen images.
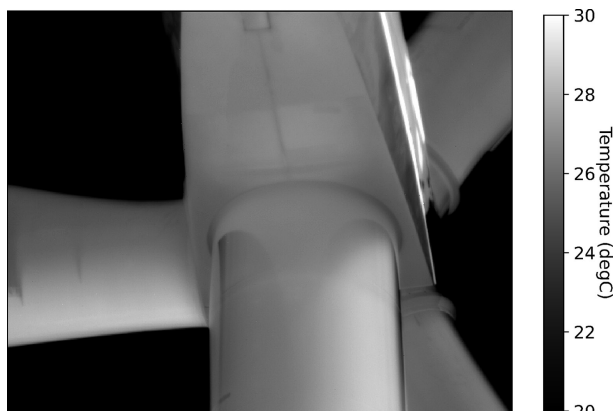
The annotations published within the dataset include not the polygons but strictly rectangular detection boxes identifying the TTP areas as determined by the CNN model. These detection boxes serve as indicators, showcasing the locations of TTP within the thermographic images. The effectiveness of the CNN in detecting and localising TTP was assessed on datasets that were not used to train the CNN. This allows an evaluation of the so-called ground truth (manual annotation of TTPs) and the CNN prediction. An example is shown in Figure 3.
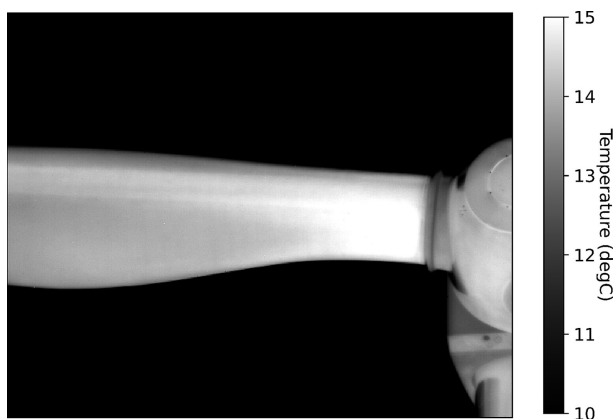

FIGURE 4 | Thermogram of a turbine captured from the suction side (SS). Filename: Turbine-3_Blade-B_Side-SS_Clock-9_No-1.

FIGURE 5 | Thermogram of a turbine captured from the pressure side (PS). Filename: Turbine-6_Blade-B_Side-PS_Clock-9_No-1.

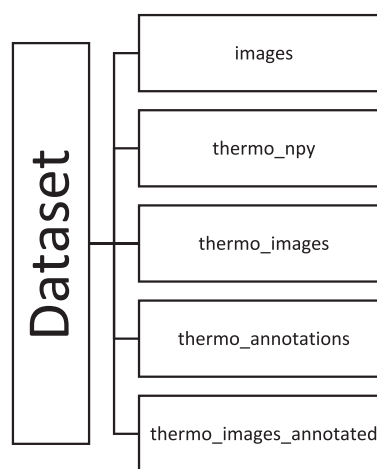**FIGURE 6** | Overview schematic of the different folders in the dataset.

TABLE 3 | Folders in the dataset.

Folder name	Description
images[a]	Contains all visual images taken with ROMOTIONCAM.
thermo_npy[b]	Contains .npy files, which are thermograms with temperature values (64-bit floating point numbers) in an array format readable with the commonly used NumPy library in the Python programming language. These files provide thermal data that complement the visual images.
thermo_images[b]	Contains the thermograms (arrays) converted to .png file format with greyscale colours. A corresponding Python function is provided, described in Section 3.3.2, which provides the possibility to also produce images with heatmap colours, apart from greyscale, as well as the possibility to add a temperature colour bar.
thermo_annotations/	Contains annotation files for the thermogram arrays (.npy format). The annotations are boxes in a .geojson format. The boxes indicate areas of thermographic turbulence patterns (TTPs).
thermo_images_annotated/	Contains the combination of thermo_images with the thermo_annotations. The corresponding function is provided, described in Section 3.3.

[a]Identification markings have been masked in the visual images.
[b]Identification markings have been changed to 'NaN' or 'not a number' values in the NumPy array and subsequently are also not visible in thermal images.

The evaluation is based on how well the CNN prediction (red) fits the ground truth (green). Commonly used metrics for evaluating AI performance were used, demonstrating its potential as a reliable tool for automatic thermographic analysis in various scientific and industrial applications:

- **Precision**: How much of the model predicted TTP pixels were actual TTP pixels: **71.87%.**
- **Recall**: How much of the actual TTP pixels were predicted by the model: **71.84%**.
- **F1-Score**: Harmonic mean of precision and recall: **71.86%**.
- **Intersection over Union (IoU)**: Measures the overlap between the prediction and ground truth in relation to their joint area: **53.15%**.

Further details of the assessment results are beyond the scope of this publication.

3 | Dataset

3.1 | Overview

This dataset comprises visual images and thermograms acquired using an infrared thermographic camera (Bundesanstalt für Materialforschung und -prüfung, BAM) and a visual inspection camera (ROMOTIONCAM). Both visual and thermographic inspections were conducted simultaneously on the same wind turbines, during their operational phase in 2023 and 2024. This approach was employed to capture the influence of damage (possibly leading edge erosion) on the transition of laminar to turbulent

TABLE 4 | Filename description.

Folder name	Description
images/	'Turbine-<*turbine_number*>_Blade-<*blade-sequence*>_Side-<*side of inspection*>_<*edge of the blade*>_No-<*blade section sequence*>.jpg' Example: Turbine-1_Blade-A_Side-SS_LE_No-1.jpg
thermo_npy/	Turbine-<*turbine_number*>_Blade-<*blade-sequence*>_Side-<*side of inspection*>_Clock-<*position of blade*>_No-<*blade section sequence*>.npy Example: Turbine-1_Blade-A_Side-SS_Clock-3_No-1.npy
thermo_images/[a]	Turbine-<*turbine_number*>_Blade-<*blade-sequence*>_Side-<*side of inspection*>_Clock-<*position of blade*>_No-<*blade section sequence*>.png Example: Turbine-1_Blade-A_Side-SS_Clock-3_No-1.png
thermo_annotations/	Turbine-<*turbine_number*>_Blade-<*blade-sequence*>_Side-<*side of inspection*>_Clock-<*position of blade*>_No-<*blade section sequence*>.geojson Example: Turbine-1_Blade-A_Side-SS_Clock-3_No-1.geojson
thermo_images_annotated/	Turbine-<*turbine_number*>_Blade-<*blade-sequence*>_Side-<*side of inspection*>_Clock-<*position of blade*>_No-<*blade section sequence*>.png Example: Turbine-1_Blade-A_Side-SS_Clock-3_No-1.png

[a]The heatmap colouring or grey scaling for the thermo_images is relative to each individual image and is provided as a colour bar with each image. The user is free to adjust this for their specific visualisation using the raw data in the NumPy array format. In this study, the coldest temperature is shown in black and the hottest in white. To enhance the visibility of even small temperature differences, the background (primarily sky and clouds) and outliers are removed prior to normalisation.

TABLE 5 | Variables used in filenames. Schematics for explaining the variables are provided in Figures 7 and 8.

Variable	Description
turbine_number	The turbine numbers from 1 to 30.
blade_sequence	Blade identification; either A, B or C.
side of inspection	The side of the turbine from which the inspection was taken; pressure side (PS) or suction side (SS).
edge of the blade	For visual images, whether the primary perspective was on the leading edge (LE) or trailing edge (TE).
blade section sequence[a]	The sequence of blade sections captured from the nacelle to the tip.
position of blade	For the thermograms, whether the position of the blade was a certain position representative of a clock (3 or 9 o'clock).

[a]The thermal images are taken in sections, as described in [21]. Because of the difference in spatial resolution of the two camera systems and blade lengths across turbines, the total number of sections per blade may differ across turbines.

flow in the thermographic images. Consequently, the dataset offers a possibility for analysing the correlation between visual and thermographic data. The dataset consists of the following:

- 30 unique wind turbines. The turbines are anonymised, that is, they are numbered as Turbines 1–30. All identification markings have been removed. Any identification of turbine type, location and so forth is unintended and purely coincidental.

- 90 blades. The blades could have either been captured from the pressure side (PS) or the suction side (SS). This is mentioned in the filename and other metadata provided. An example of each is given in Figures 4 and 5.

- 2160 visual images, each in .jpg format and 5400×7920 pixels. All identification markings have been removed.

- 1206 thermograms, each an array of 640×512 (64-bit floating-point number) temperature values in degrees Celsius. Thus, the original thermal data are provided (used temperature calibration of the IRT camera: $-10°C$ to $+40°C$). All identification markings have been removed.

3.2 | Dataset Management

The distribution of the data is provided in this section, along with the strategies used for setting the filename. Based on the AI-based detection described in Section 2.2, the TTPs detected in the thermograms have been annotated and provided in the dataset.
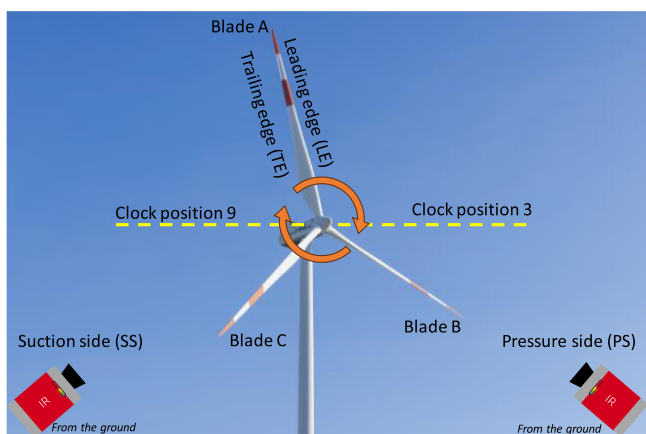
3.2.1 | Folders

The main folder is titled 'ki-visir_dataset_v1'. The remaining folders are described in Table 3. An overview schematic of the different folders can be seen in Figure 6.

3.2.2 | Filename Strategies

For naming the data files, the strategy is described in Table 4. The variables used are described in Table 5. Two schematics are provided in Figures 7 and 8 that visually represent the variables for ease of interpreting.

3.3 | Provided Tools

3.3.1 | Metadata

Metadata corresponding to the dataset have been provided in a comma-separated file (.csv). Each thermogram and visual image has been referred to in this .csv file to provide the user with additional information regarding the inspection. The columns in the metadata are described in Table 6 where an example is given for the filename 'Turbine-6_Blade-A_Side-PS_Clock-9_No-1', which is shown in Figure 5.

3.3.2 | Python Programming Functions

In addition to metadata, a few Python programming functions have been provided in the 'ki_visir_helper_functions_v2.py' file that provides users a 'quick start' way of using the dataset. The functions provided are briefly explained in Table 7. The script is well-commented to leave as little as possible to interpretation. Basic knowledge of Python and basic Python package installation on a computer are required.

4 | Discussion

The dataset indicates the possibility of capturing thermal turbulence patterns (TTPs) that may act as an indication to wind

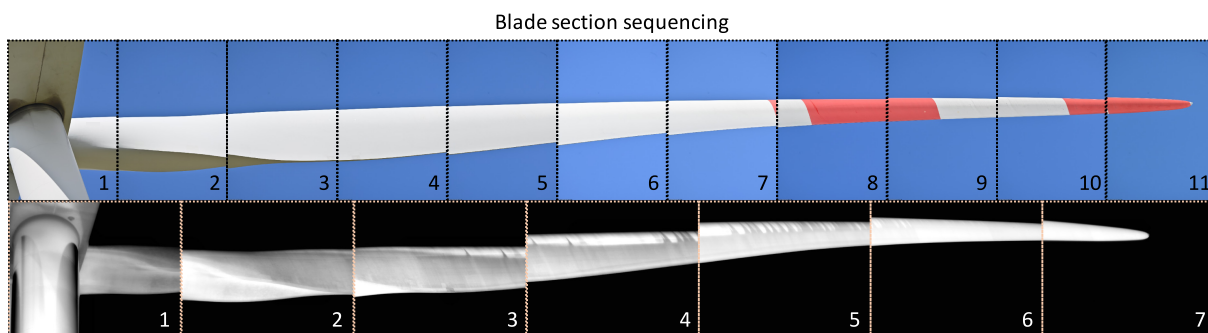**FIGURE 7** | Schematic to visualise variables linked to data management.

FIGURE 8 | Blade section sequencing example for visual and thermal images. Images from Turbine-2 Blade B Suction side in the dataset.

turbine operators that the rotor blades may have some additional aerodynamic losses due to the drag generated. The TTPs can also be identified using an AI-based algorithm. It should be noted that the measured temperatures on the rotor blade depend on the following parameters:

1. internal structure of the rotor blades as well as thermal properties of the used materials;

2. solar irradiation and reflections from the sun, sky and ground;

3. convection depending on the air flow on the rotor blade (laminar/turbulent);

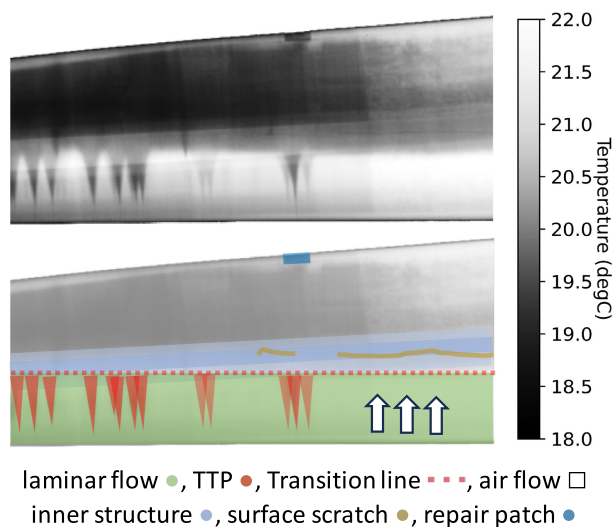4. surface emissivity, which is influenced by the paintwork as well as dirt.

TABLE 6 | Columns in the metadata file.

Column title	Description	Example (see Figure 5)
turbine	Identifier for the turbine	Turbine-6
bladelength_m	Length of the blade in metres	38
blade	Identifier for the blade (A, B C)	B
blade_side	Side of the blade being inspected (Suction Side (SS)/Pressure Side (PS))	PS
inspection_type	Type of inspection performed (image/thermo)	thermo
blade_view	Only for visual inspection: the view angle or perspective of the blade in the image (Leading Edge (LE)/Trailing Edge (TE))	—
clock_position	Only for thermograms: Position of the blade in terms of clock orientation (3/9 o'clock)	9
group	Unique name for each set of visual and thermal blade inspection data	Turbine-6_B_PS
file_sequence	Sequence identifier for images/thermograms. A sequence is a set of images that belong together and illustrate a whole blade_side	85
image_order	Order of the image in the inspection sequence. Goes from left to right for visual inspections and 3 o'clock thermograms. Goes from right to left for 9 o'clock thermograms (always from the hub to the tip of the blade)	1
file_name	Name of the image or thermogram file	Turbine-6_Blade-B_Side-PS_Clock-9_No-1
left_blade_m[a]	Blade section at the left image border in metres. (root = 0, tip = blade length)	0.12
center_blade_m[a]	Blade section at the image centre in metres. (root = 0, tip = blade length)	4.02
right_blade_m[a]	Blade section at right image border in metres. (root = 0, tip = blade length)	7.92
same_time_image_and_thermo	Indicates if the image and thermogram were taken at the same time (True/False)	TRUE
wind_conditions_kmh	Wind conditions in kilometres per hour during the inspection	14
weather_conditions	General weather conditions during the inspection	Mostly Cloudy
humidity_rhpercent	Relative humidity percentage during the inspection	50
temperature_c	Temperature in Celsius during the inspection	19
comment	Additional comments or notes about the inspection	—

[a]The variables [left_blade_m, center_blade_m, right_blade_m] may lack precision because of factors such as blade or nacelle movements. Because these parameters are used to calculate the actual rotor blade section shown (length X metres to Y metres) for each image, the overlap between two adjacent images can then be calculated. Generally, the values obtained from visual inspections tend to be more accurate than those from thermographic inspections.

TABLE 7 | Python functions provided with the dataset.

Function	Description
npy_to_image	Convert a NumPy array to a greyscale or heatmap image. Returns a 3D NumPy array each representing the RGB colour channels.
convert_npy_folder_to_png	Convert all .npy files in a folder to .png images with either greyscale or heatmap colour maps.
combine_images	Combines multiple images into a single large image (for ease of viewing) for a specified group. Used within the next function.
combine_images_by_group	Performs the combine_images function based on groups in the metadata.
draw_geojson_on_images	Draw polygons from GeoJSON files onto corresponding PNG images and save the results.

laminar flow ●, TTP ●, Transition line ▪ ▪ ▪, air flow □
inner structure ●, surface scratch ●, repair patch ●

FIGURE 9 | Top: Thermogram of a rotor blade section in operation. Bottom: The same thermogram with annotated features. Filename: Turbine-2_Blade-B_Side-SS_Clock-9_No-3.

It is thus evident that the laminar flow on the rotor blade is only one of many effects that influence the measured surface temperature and that the other effects should always be taken into account when interpreting the measured temperatures. This is because thermographic measurements are also used, in other cases, to visualise the internal structures of rotor blades at standstill or in idle mode. Figure 9 shows a thermographic image of a running rotor blade. The various influences on the measured surface temperature can be clearly recognised in this figure. In addition to the TTPs, which run as triangles from the leading edge (bottom) in dark (low temperature), inner structure (spar and repairs) and surface features (scratches) are recognisable in the thermogram.

5 | Summary

The presented dataset contains the thermographic and visual images of 30 wind turbines taken simultaneously and from the same position relative to the rotor blades (see schematic in Figure 1 for reference). This results in visual and thermal images that have the same perspective of the rotor blades, allowing a direct spatial comparison of the acquired images. The focus of the measurements is to thermally visualise the transition from laminar to turbulent flow due to possible leading edge erosion, amongst other damage mechanisms. The dataset is free to download from https://www.doi.org/10.5281/zenodo.13771900. This short communication document may act as an aid for the user to understand how the data have been managed and may guide the user to a 'quick-start' with the data. More on the algorithm and analysis of the TTP will be available in a follow-up article.

Author Contributions

Somsubhro Chaudhuri: methodology, project administration, software, hardware, data curation, inspection, validation, formal analysis, writing – original draft, visualisation. **Michael Stamm**: conceptualisation, resources, project administration, funding acquisition, methodology, writing – reviewing and editing. **Ivana Lapšanská**: hardware, inspection, data curation, writing – reviewing and editing. **Thibault Lançon**: inspection, data curation. **Lars Osterbrink**: software, data curation, validation, formal analysis, writing – reviewing and editing. **Thomas Driebe**: software, data curation, validation, formal analysis. **Daniel Hein:** conceptualisation, project management. **René Harendt**: hardware, inspection, data curation, formal analysis, writing – reviewing and editing.

Conflicts of Interest

The authors declare no conflicts of interest.

Data Availability Statement

https://www.doi.org/10.5281/zenodo.13771900

Peer Review

The peer review history for this article is available at https://www.webofscience.com/api/gateway/wos/peer-review/10.1002/we.2958.

References

1. (GWEC), G.W.E.C, *Global Wind Report* (Brussels, Belgium: GWEC, 2023), https://gwec.net/globalwindreport2023/.

2. B. A. Lobo, Ö. S. Özçakmak, H. A. Madsen, A. P. Schaffarczyk, M. Breuer, and N. N. Sørensen, "On the Laminar–Turbulent Transition Mechanism on Megawatt Wind Turbine Blades Operating in Atmospheric Flow," *Wind Energy Science* 8 (2023): 303–326, https://doi.org/10.5194/wes-8-303-2023.

3. A. P. Schaffarczyk, D. Schwab, and M. Breuer, "Experimental Detection of Laminar-Turbulent Transition on a Rotating Wind Turbine Blade in the Free Atmosphere," *Wind Energy* 20 (2017): 211–220, https://doi.org/10.1002/we.2001.

4. D. M. Eggleston and K. Starcher, "A Comparative Study of the Aerodynamics of Several Wind Turbines Using Flow Visualization," *Journal of Solar Energy Engineering* 112 (1990): 301–309, https://doi.org/10.1115/1.2929938.

5. A. Sareen, C. A. Sapre, and M. S. Selig, "Effects of Leading Edge Erosion on Wind Turbine Blade Performance," *Wind Energy* 17 (2014): 1531–1542, https://doi.org/10.1002/we.1649.

6. F. Jensen, J. F. Jerg, M. Sorg, and A. Fischer, "Active Thermography for the Interpretation and Detection of Rain Erosion Damage Evolution on GFRP Airfoils," *NDT & E International* 135 (2023): 102778, https://doi.org/10.1016/j.ndteint.2022.102778.

7. F. Jensen, E. A. Aoun, O. Focke, et al., "Investigation of the Causes of Premature Rain Erosion Evolution in Rotor Blade-Like GFRP Structures by Means of CT, XRM, and Active Thermography," *Applied Sciences* 12 (2022): 11307, https://doi.org/10.3390/app122211307.

8. A. S. Verma, S. G. P. Castro, Z. Jiang, and J. J. E. Teuwen, "Numerical Investigation of Rain Droplet Impact on Offshore Wind Turbine Blades Under Different Rainfall Conditions: A Parametric Study," *Composite Structures* 241 (2020): 112096, https://doi.org/10.1016/j.compstruct.2020.112096.

9. H. Law and V. Koutsos, "Leading Edge Erosion of Wind Turbines: Effect of Solid Airborne Particles and Rain on Operational Wind Farms," *Wind Energy* 23 (2020): 1955–1965, https://doi.org/10.1002/we.2540.

10. L. Mishnaevsky, A. Tempelis, N. Kuthe, and P. Mahajan, "Recent Developments in the Protection of Wind Turbine Blades Against Leading Edge Erosion: Materials Solutions and Predictive Modelling," *Renewable Energy* 215 (2023): 118966, https://doi.org/10.1016/j.renene.2023.118966.

11. W. Han, J. Kim, and B. Kim, "Effects of Contamination and Erosion at the Leading Edge of Blade Tip Airfoils on the Annual Energy Production of Wind Turbines," *Renewable Energy* 115 (2018): 817–823, https://doi.org/10.1016/j.renene.2017.09.002.

12. Y. Zhang, F. Avallone, and S. Watson, "Leading Edge Erosion Detection for a Wind Turbine Blade Using Far-Field Aerodynamic Noise," *Applied Acoustics* 207 (2023): 109365, https://doi.org/10.1016/j.apacoust.2023.109365.

13. F. Jensen, M. Sorg, A. von Freyberg, N. Balaresque, and A. Fischer, "Detection of Erosion Damage on Airfoils by Means of Thermographic Flow Visualization," *European Journal of Mechanics - B/Fluids* 104 (2024): 123–135, https://doi.org/10.1016/j.euromechflu.2023.12.004.

14. J. Dieckmann, C. Dorszewski, N. Balaresque, A. von Freyberg, and A. Fischer, "Bayesian-Based Approach for the Thermographic Measurement of Flow Transition on Wind Turbine Rotor Blades," *Applied Sciences* 14 (2024): 1166, https://doi.org/10.3390/app14031166.

15. D. Gleichauf, F. Oehme, A. M. Parrey, M. Sorg, N. Balaresque, and A. Fischer, "On-Site Contactless Visualization of the Laminar-Turbulent Flow Transition Dynamics on Wind Turbines," *Tm - Technisches Messen* 90 (2023): 613–623, https://doi.org/10.1515/teme-2022-0120.

16. A.-M. Parrey, D. Gleichauf, M. Sorg, and A. Fischer, "Automated Detection of Premature Flow Transitions on Wind Turbine Blades Using Model-Based Algorithms," *Applied Sciences* 11 (2021): 8700, https://doi.org/10.3390/app11188700.

17. I. Kaufmann, C. Scherer-Klöckling, and H. Nawrocki, *Patent 102017219153A1: Vorrichtung und Verfahren zur optischen Überwachung bewegter Bauteile* (Germany: Deutches Patent- und Markenamt, 2019).

18. P. Hidayatullah and R. Tubagus. *YOLOv9 Architecture Explained|Stunning Vision AI*, accessed 16 Sep 2024, https://article.stunningvisionai.com/yolov9-architecture.

19. C.-Y. Wang and H.-Y.M. Liao. *yolov9*, https://github.com/WongKinYiu/yolov9.

20. C.-Y. Wang and H.-Y.M. Liao, "*YOLOv9: Learning What You Want to Learn Using Programmable Gradient Information*", 2024 https://doi.org/10.48550/arXiv.2402.13616.

21. M. Doroshtnasir, T. Worzewski, R. Krankenhagen, and M. Röllig, "On-Site Inspection of Potential Defects in Wind Turbine Rotor Blades With Thermography," *Wind Energy* 19 (2016): 1407–1422, https://doi.org/10.1002/we.1927.